Enhancing H₂ production rate in PGM-free photoelectrochemical cells by glycerol photo-oxidation

*Claudio M. Pecoraro, Francesco Di Franco, Marianna Bellardita, Vittorio Loddo, Monica Santamaria**

Dipartimento di Ingegneria, Università degli Studi di Palermo, Viale delle Scienze Edificio 6, 90128 Palermo, Italy

HIGHLIGHTS

- Photoelectrocatalytic H₂, DHA, and GA production by glycerol reforming were studied.
- TiO₂ NTs on Ti foil or Ti fiber felt, and Pt-free Ni foam were used as photoanode and cathode respectively.
- H₂ faradaic efficiency of 100% was obtained.
- Electrodes were reused for each test showing good mechanical properties and photostability.

GRAPHICAL ABSTRACT
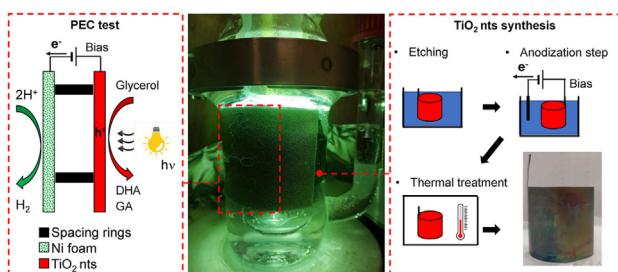
ABSTRACT

The photo-oxidation of glycerol was carried out by using TiO₂ NTs photoanodes and Ni foam as the cathode for the Hydrogen Evolution Reaction. The photoanodes were prepared by anodizing Ti foils and titanium felt and then annealed under air exposure. They were tested in acidic aqueous solution without and with the addition of glycerol. When glycerol was present, the hydrogen production rate increased and allowed the simultaneous production of high value added partial oxidation compounds, i.e. 1,3-dihydroxyacetone (DHA), and glyceraldehyde (GA). The highest H₂ evolution and partial oxidation compounds production rates were obtained by using home prepared TiO₂ nanotubes (TiO₂ NTs) synthesized on Ti fiber felt as the photoanode with an irradiated area of 90 cm². These photoanodes were found to be highly stable both from a mechanical and a chemical point of view, so they can be reused after a simple cleaning step.

* Corresponding author.
E-mail address: monica.santamaria@unipa.it (M. Santamaria).

1.   Introduction

In recent years, the depletion of non-renewable resources, climate changes, and local pollution are dramatically changing the methods of energy generation. Among them, hydrogen production is one of the options in the decarbonization of chemical processes [1–5]. Moreover, the manufacture of green hydrogen via water electrolysis is the way to transition from the consumption of fossil fuels to the clean energy of the future [6,7]. Indeed, it is linked to solar and wind energy production that far exceeds the global energy demand today and in any future scenario. Moreover, it is the only zero-carbon option for hydrogen production, as Carbon Capture and Storage (CCS) has at the best efficiency of 85%–95% [8,9].

However, there are still some challenges that need to be addressed to make it sustainable from an economic and environmental point of view. For instance, one of them is the use of Platinum Group Metal (PGM) free catalysts, since Pt manufacturing is energy demanding and responsible for greenhouse gases emission. Others are the improvement of the kinetics of the Oxygen Evolution Reaction (OER) anode side, and the minimization of the energy consumption of the overall system [10–13]. Indeed, OER is a slow reaction that needs a very high overvoltage to be activated even in the presence of catalysts and poses several restrictions in catalyst selection due to the very positive operating voltage which could cause very severe corrosion issues at this electrode [14–16].

Adding in the solution species that can compete with water oxidation and have a less demanding kinetic can be an effective strategy to minimize the overall energy consumption during the electrolysis [17–20]. Biomass is a good candidate since the corresponding oxidation products could be high-value-added molecules that find application as intermediates for plastics, pharmaceuticals, and textiles [20–27].

The catalytic oxidation of glycerol, a surplus byproduct of biodiesel production, has received increasing attention due to the significant applications of its oxygenated compounds, such as aldehydes, ketones, and carboxylate species [28–30]. Among the products, 1,3-dihydroxyacetone (DHA) is one of the most valuable since it is widely used in cosmetic, pharmaceutical, fine chemical, and food industries. The price of DHA is ~US $150 per kg, whereas the prices of crude and refined glycerol are much lower (US $0.11 and US $0.66 per kg, respectively), making catalytic production of DHA from glycerol an economically attractive method [31,32].

Generally, the industrial production of DHA starting from glycerol is mainly based on a thermocatalytic oxidation process, which employs costly noble-metal catalysts (such as Pt, Au, Pd) with exogenous oxidants (e.g., O_2, H_2O_2) and severe reaction conditions [33–35]. Recently, to convert glycerol to DHA under mild conditions an electrocatalytic method, ideally sustainable if a renewable energy source (e.g., solar energy, wind) is selected to supply the electricity, has been proposed [36]. However, noble metals such as Pt and Pd are still needed to obtain high selectivity toward DHA.

Moreover, a way to minimize energy consumption can be the use of light as a source of energy. For example, photoelectrocatalysis, which couples photocatalysis (PC) and electrocatalysis (EC), is based on semiconductor photoelectrodes irradiated by light with suitable energy (higher or equal to that of its band gap) and contemporaneously biased by an electrical potential [37,38]. Therefore, there is a photoanode where the anodic half-cell reaction can occur and a cathode where the reduction half-cell reaction takes place [39–46]. This method represents a sustainable and energy-saving way for the production of value-added chemicals by partial oxidation of cheap organic molecules and simultaneously promotes the cathodic H_2 production [47,48]. The selection of a photoanode with a suitable valence band (VB) potential is very important to enhance the selectivity towards DHA, while Pt-based cathodes are usually employed to get a good H_2 evolution rate with low overvoltage [24,49–52].

Although various semiconductors have been tested as photoanode, TiO_2 is the most widely employed photocatalyst because it is cheap and photostable. Consequently, these electrodes can be used many times without being damaged, and the recovery of the catalyst from the reaction medium is very easy [53–56].

In their work, Cetinkaya et al. [36] studied the PEC oxidation of glycerol by using different TiO_2 geometries, obtaining glycerol conversions up to 37% and selectivity toward DHA and GA of 6% and 13% respectively after 3 h of reaction using TiO_2 NTs, and applying 1.5 V vs Ag/AgCl. Luo et al. [33] achieved high-selective PEC oxidation of glycerol to DHA by using a Bi_2O_3/TiO_2 photoanode, obtaining a glycerol conversion rate of up to 228 mmol $m^{-2} h^{-1}$ at 1.0 V vs RHE and selectivity towards DHA up to 75.4% with a faradaic efficiency (FE) of 62.2%.

In this work, hydrogen production by glycerol photo-reforming and water splitting on TiO_2 nanotubes photoanode was studied with a specific focus on electrode surface engineering to enhance the hydrogen evolution rate and evaluate the faradaic efficiency (FE) towards DHA and glyceraldehyde (GA) production. The photoanode was prepared by anodizing Ti foil or Ti felts with a high specific surface area further enhanced by TiO_2 NTs. PGM-free cathodes were used as a low-cost alternative compared to the noble metal-based catalysts and they were able to overcome possible poisoning effects due to the presence of organic species [57].

2.   Experimental

2.1.   *Electrodes preparation*

Previous studies [58–60] showed that TiO_2 NTs photoanodes can be prepared by anodizing processes. Titanium foils (Sigma Aldrich, purity >99.7%) with 0.127 mm thickness or Titanium fiber felt (Fuel cell store) with 0.2–0.3 mm thickness were properly cut and etched, 15 or 5 s, respectively, in a mixture of hydrofluoric acid (Sigma Aldrich, purity 39.5%), nitric acid (Sigma Aldrich, purity 69.0%) and deionized water with a volume ratio of 1:1:3. Then, they were cleaned by sonication in acetone and ethanol for 5 min each, rinsed with deionized water, and dried in air. TiO_2 NTs were formed in ethylene glycol (Aldrich, 99.8% anhydrous) solution containing 0.25 wt % NH_4F (Sigma Aldrich) and 0.75 wt% deionized water. The anodizing process was carried out in a two-electrode cell

configuration, by using aluminum foil as the cathode. The potential was kept constant during anodizing at 45 V for 5, 10, or 20 min. After that, a thermal treatment was performed to induce the crystallization of the TiO_2 NTs. In particular, to optimize the synthesis procedure, the layers were heated in air to 450 °C for 3 h or 550 °C for 12 h respectively, and left to cool inside the oven. A relatively low annealing time was chosen to have a thin and not very blocking thermally induced titanium oxide layer between the bare titanium and the nanotubes.

Commercial Ni foam (Goodfellow) was used as the cathode.

2.2. Characterizations

Thermodynamics and kinetics of the partial oxidation of glycerol were studied through cyclic voltammetry in 0.5 M Na_2SO_4 (Sigma-Aldrich, ≥99%) aqueous solution without and with 0.1 M glycerol (Sigma-Aldrich, ≥99.5%) concentrations. The pH was adjusted to 2 by adding H_2SO_4 (Sigma-Aldrich, 97%) dropwise. Cyclic voltammetry was recorded between 0 and 2 V vs Ag/AgCl, by using a three-electrode cell configuration with Pt mesh as the working and counter electrode and Ag/AgCl/3.5 M KCl as the reference one. The scan rate was 5 mV/s and a Parstat 2263 potentiostat was used.

Scanning electron microscopy (SEM) images were obtained by using a FEI Quanta 200 ESEM microscope operating at 30 kV. An electron microprobe used in an energy dispersive mode (EDX) was employed to obtain information on sample composition.

X-Ray diffraction (XRD) patterns of the photoanodes were acquired at room temperature by a PANalytical Empyrean diffractometer equipped with a PIXcel1D (tm) detector working at a voltage of 40 kV and a current of 40 mA and using the CuKα radiation and a 2θ scan rate of 3°/min.

Raman spectra were collected by a Raman Microscope coupled with a Leica DMLM microscope. The laser has been focused on the sample by a 5× magnification lens to obtain an analyzing spot diameter of around 50 μm, with a maximum laser power of 133 mW. Only the 10% of maximum power has been used in these measurements, the power was reduced by holographic filters, three for each sample, and the spectra have been recorded using a 532 nm laser coupled with 2400 lines per millimeter grating resulting in a spectral resolution equal to 0.5 cm^{-1}. Every measurement consists of two accumulations.

For the photoelectrochemical measurements, TiO_2 NTs on Ti felt photoanode was used as the working electrode in a three-electrode configuration cell, a Pt wire was used as the counter electrode, and a silver/silver chloride (Ag/AgCl/sat. KCl) was employed as the reference electrode. 0.5 M Na_2SO_4 aqueous solution was used as the electrolyte, and the pH was adjusted to 2 by adding H_2SO_4 dropwise [31].

Electrochemical Impedance Spectroscopy (EIS) measurements were carried out using a Parstat 2263 potentiostat equipped with an Impedance Analyzer connected to the cell. The impedance spectra were recorded in the range 10 kHz - 0.1 Hz at 25 °C and an ac amplitude of 10 mV. Before each measurement, the cell was stabilized for at least 15 min under irradiation. The data analysis and equivalent circuit fitting

were carried out through a Power Suite and ZSimpleWin software.

2.3. Photoelectrocatalytic tests

Photoelectrocatalytic tests were carried out by using TiO_2 NTs as photoanode, Ni foam as cathode, and Na_2SO_4 as the electrolyte. The pH was 2 (adjusted with H_2SO_4) and the applied potential between the photoanode and cathode was 1 V. The glycerol initial concentration was in the range of 0–0.5 M.

The reaction was carried out in the undivided glass cells shown in Fig. 1 with a two electrodes configuration. As far as the irradiation is concerned, a Hg medium-pressure lamp with a maximum near-UV wavelength of 365 nm (125 W) was used. The photoanodes and the cathode with 24 cm^2 (irradiated) and 8 cm^2 surface, respectively were used to determine the TiO_2 NTs on Ti foil performances by varying the synthesis conditions, i.e., anodization time and thermal treatment. After this optimization, the best sample was tested by scaling up the photoanodes and the cathode surface up to 90 cm^2 (irradiated) and 180 cm^2, respectively. Moreover, improvements were obtained by using Titanium fiber felt as support instead of Titanium foil and increasing the glycerol initial concentration.

A Parstat 2263 (PAR) equipped with the facilities for Electrochemical Impedance Spectroscopy (EIS) was used to control the cell potential and to collect kinetic data of both anodic and cathodic processes.

Before each run, Helium was bubbled under stirring in the dark for 30 min in the glycerol aqueous solution, both to remove oxygen from the system and to saturate the electrode's surface by the substrate, then the reactor was closed, and the lamp switched on. Runs were carried out for 5 h at room temperature by circulating water in the reactor cooling jacket.

The photoanode was reused after sonication with acetone and water for 5 min each to remove any residues of glycerol, while Ni foam was cleaned by sonication for 5 min in 1 M HCl.

2.4. Analytical techniques

The identification and quantification of glycerol and reaction intermediates were performed by using a Thermo Scientific Dionex UltiMate 3000 HPLC equipped with a Diode Array detector and a REZEK ROA Organic acid H^+ column. Gaseous species accumulated in the reactor headspace were analyzed by an HP 6890 Series GC system equipped with a Supelco GC 60/80 CarboxenTM-1000 packed column and a thermal conductivity detector.

For DHA, GA, and CO_2, the faradaic efficiency was calculated through Eqn. (1):

$$Faradaic\ efficiency_i\ [\%] = \frac{Amount\ of\ product\ i\ formed\ [mol]}{\frac{Q\ [Couloumb]}{z\ F\ [Couloumb/mol]}} \times 100$$

(1)

where.

- i is the formed product
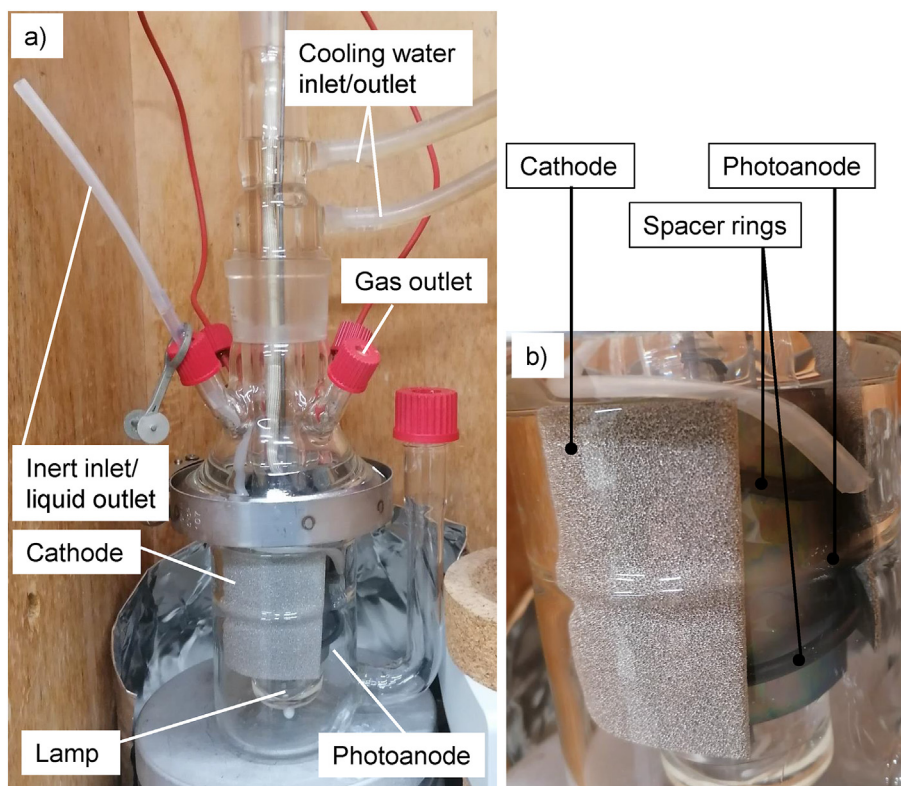- Q is the circulated charge

Fig. 1 – Pictures of a) PEC system with a photoanode irradiated area of 90 cm2 and b) magnification of photoanode and cathode layout.

- z are the electrons exchanged, that are equivalent to the number of holes shown in Eqns. (2) and (3)
- F is the Faraday constant of 96,485 [Couloumb/mol]

3. Results and discussion

A preliminary electrochemical investigation was carried out to obtain information about the kinetic of glycerol oxidation in aqueous solution. Fig. 2a shows the cyclic voltammetry recorded in glycerol-free and glycerol-containing 0.5 M Na_2SO_4 solution at pH 2 by using a Pt mesh as the working electrode. The Faradaic current, attributed to the glycerol oxidation, starts to circulate by increasing the potential toward the positive direction (see inset of Fig. 2a). Indeed, in glycerol-free solution the onset potential for the circulation of a Faradaic current (due to OER) is higher, suggesting that glycerol oxidation is kinetically favorable.

This finding is also supported by the EIS spectra recorded in 0.5 M Na_2SO_4 at pH 2 without (Fig. 2c and d) and with the addition of glycerol (Fig. 2e and f).

In Table 1 are reported the parameters of the equivalent circuit in Fig. 2b, related to the EIS spectra shown in Fig. 2c–f. R_s is the solution resistance, R_{ct} is the charge transfer resistance, and $Q_{DL,el}$ accounts for the double-layer capacitance.

R_s and $Q_{DL,el}$ are practically the same as the potential varies and are not affected by the presence of glycerol. A very high charge transfer resistance (in the order of 10^5 Ω cm^2) was estimated at the equilibrium potential for oxygen evolution (i.e. ~ 0.9 V vs Ag/AgCl) and at an even higher potential (1.1 V vs Ag/AgCl) in the absence of glycerol (Table 1a). Conversely, when glycerol is present in the electrolytic solution, at the lowest potential values, its oxidation allows lower charge transfer resistance. On the contrary, at higher potentials, in the presence of glycerol and its partial oxidation products, higher charge transfer resistance and lower current density occur, probably due to their strong adsorption on the Pt surface (see Fig. 2a).

3.1. Photoanode preparation

Fig. 3 shows the SEM images of TiO_2 NTs after anodizing and thermal treatment. The micrographs clearly show the successful formation of a large array of TiO_2 NTs (Fig. 3a and b) with an average length range of ~350 nm–~1.22 μm when the anodization time increases from 5 to 20 min, respectively. These results agree with previous studies on flat titanium sheets [58]. Conversely, NTs length is not affected by the time and temperature of thermal treatment (i.e. 3 h at 450 °C (Fig. 3c and d) and 12 h at 550 °C (Fig. 3e)) or the use of Ti felt instead of Ti foil (Fig. 3f and g respectively).

XRD patterns in Fig. 4 show peaks related to TiO_2 anatase and rutile phases and bare titanium [61]. As shown in Fig. 4a, a more evident peak of the rutile phase is present when the thermal treatment was carried out at a higher temperature and longer time in agreement with previous results reported

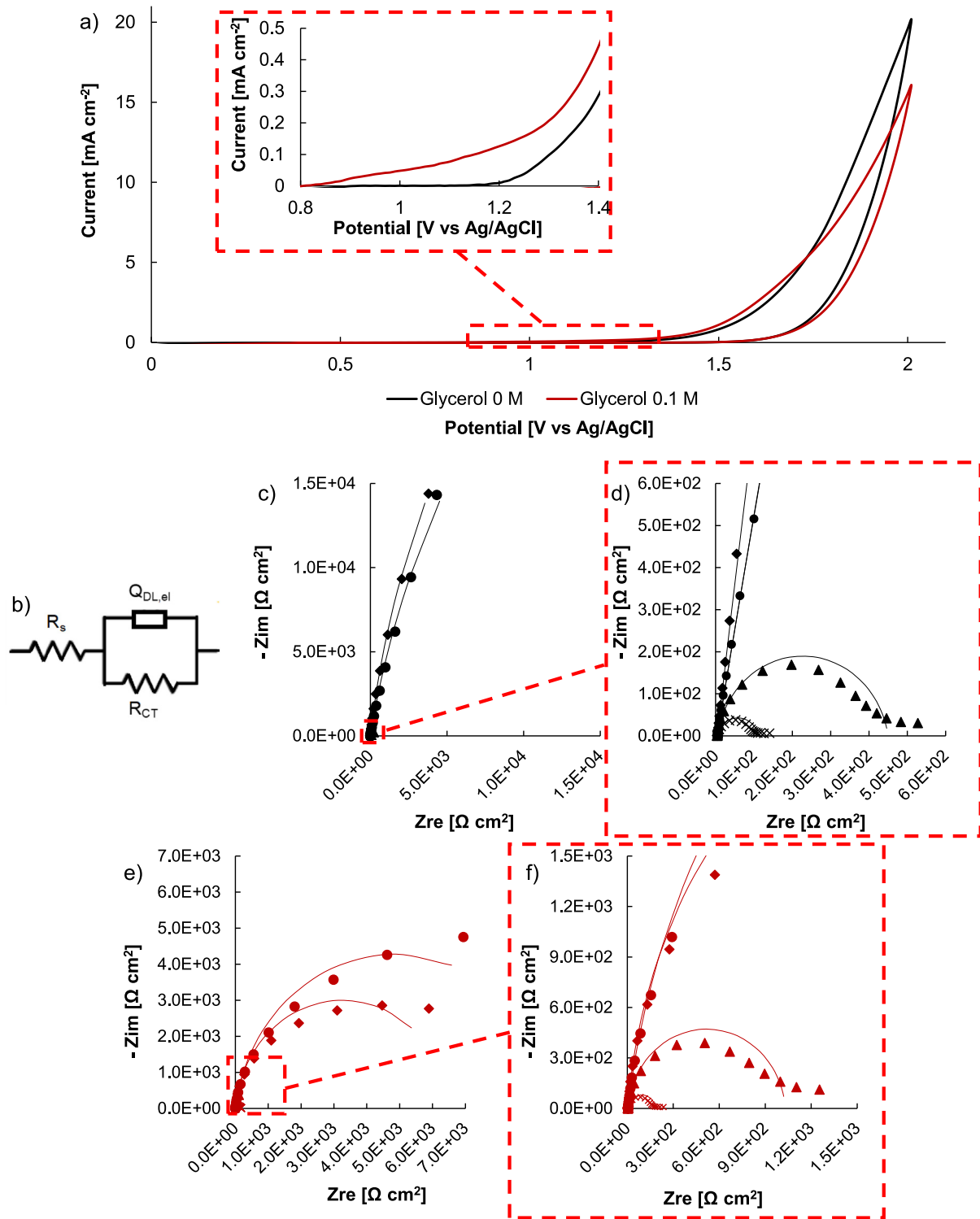Fig. 2 — Cyclic voltammetry using Pt as the counter and the working electrode, recorded at 5 mV/s without and with 0.1 M glycerol in 0.5 M Na_2SO_4 and pH 2, black and red lines respectively. EIS spectra recorded without, and 0.1 M glycerol are reported in c) - d) and e) − f) respectively. Spectra recorded at (●) 0.9, (◆) 1.1, (▲) 1.3, and (x) 1.5 V vs Ag/AgCl were fitted using the equivalent circuit shown in b).

Table 1a — Fitting parameters of EIS spectra recorded in 0.5 M Na₂SO₄ at pH 2 using Pt mesh as the counter and the working electrode recorded at various potentials without glycerol.

Applied potential [V vs ag/AgCl]	R_s [Ω cm^2]	R_{ct} [Ω cm^2]	$Q_{DL,el}$ [S s^n cm^{-2}]	n	χ square [adm]
0.9	3.99	$1.06 \cdot 10^5$	$9.95 \cdot 10^{-5}$	0.887	$7.23 \cdot 10^{-4}$
1.1	4.2	$1.11 \cdot 10^5$	$1.05 \cdot 10^{-4}$	0.921	$1.43 \cdot 10^{-3}$
1.3	4.1	446	$1.4 \cdot 10^{-4}$	0.898	$4.52 \cdot 10^{-3}$
1.5	3.89	101	$1.94 \cdot 10^{-4}$	0.853	$8.53 \cdot 10^{-3}$

in the literature [62]. According to previous works, due to the annealing treatment following the anodizing process, two phenomena occur simultaneously. Amorphous TiO₂ of the nanotubes becomes anatase, while at the titanium/nanotube interface, a thermal oxidation process occurs involving the not anodized substrate to form rutile. The latter allows also a strong adhesion between the NTs and the metallic substrates. A thermal treatment at 450 °C under air exposure for 3h induces the formation of 140 nm thick rutile layer. Moreover, the tube wall mainly consists of anatase crystals with a cylindrical shape that can be several hundred nanometers long in the direction of the nanotube axis [63,64].

No evident TiO₂ peaks were detected for NTs synthesized on Ti felt, only a small peak at ~40° related to Ti is present, probably due to the different orientations of the nanotubes along the Ti felt fibers.

Raman spectra in Fig. 5 show characteristic bands of anatase at 144 cm^{-1}, 196 cm^{-1}, 397 cm^{-1}, 513 cm^{-1}, and 639 cm^{-1} and rutile at 447 and 612 cm^{-1} [65]. As confirmed by XRD patterns in Fig. 4 rutile phase appears by increasing temperature and time of the thermal treatment [24], while no differences were observed using Ti felt as substrate. A slight shift in the peak at ca. 144 cm^{-1} can be noticed for some of the samples ascribable to the presence of oxygen vacancies in the TiO₂ structure [66].

Photoelectrochemical measurements were carried out to study the electronic properties of the photocatalysts. The photocurrent spectrum (i.e. photocurrent vs wavelength curve) recorded in 0.5 M Na₂SO₄ at pH 2 at 0.5 V vs Ag/AgCl reported in Fig. 6a shows a maximum photocurrent value at ca. 320 nm. By assuming non-direct optical transitions, it is possible to estimate an optical band gap value, E_g, by extrapolating to zero $(Q_{ph} \cdot h\nu)^{0.5}$ vs $h\nu$ plot (see Fig. 6b. E_g is 3.05 eV, lower than that reported for anatase (i.e. 3.2 eV, [58,67]). This finding can be due to optical transitions related to the presence of allowed localized states inside the gap. Indeed, thermal treatment induces the formation of a sub-stoichiometric oxide TiO₂₋ₓ with oxygen vacancies responsible for the previously mentioned localized states. Current transients were recorded under monochromatic irradiation (λ = 320 nm) at several constant potentials. The photocurrent was measured

by manually stopping the irradiation at applied potential varying from 1 to −0.75 V vs Ag/AgCl (see Fig. 6c). An anodic photocurrent was measured confirming the n-type semiconductor behavior of the oxide, and the photocurrent was zero at ~ −0.75 V vs Ag/AgCl, that can be therefore assumed as an estimate of the flat band potential, V_{fb}. This value is more cathodic if compared to other results reported in the literature [67] in agreement with a high concentration of oxygen vacancies whose presence generates an empty allowed localized state close to the conduction band edge [68].

3.2. Photoelectrochemical tests

Several TiO₂ NTs photoanodes were prepared by changing the anodizing time (and consequently the NTs length) and the thermal treatment temperature. Their activity was evaluated in aqueous solutions without and with the addition of glycerol. The analysis of the reaction mixture composition and the gaseous stream produced at the anode provided information about the obtained products with specific interest to those derived by glycerol oxidation. Among them, it was possible to identify DHA, GA, and CO₂ corresponding to the following half-cell reactions in Eqns. (2) and (3):

$$Ox : C_3H_8O_3 + 2\,h^+ \rightarrow C_3H_6O_3 + 2\,H^+ \tag{2}$$

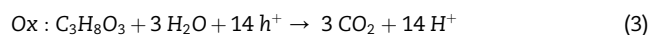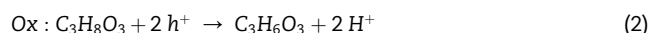$$Ox : C_3H_8O_3 + 3\,H_2O + 14\,h^+ \rightarrow 3\,CO_2 + 14\,H^+ \tag{3}$$

Table 2 summarizes the results obtained by using a photoanode irradiated surface of 24 cm². As it can be noticed, in the same experimental conditions, the addition of glycerol enhances the measured photocurrent by ~30%, thus suggesting that glycerol photo-oxidation occurs in parallel with oxygen evolution. Notably, the enhanced photocurrent due to glycerol oxidation resulted in a higher H₂ production.

As suggested by the data of Table 2, the optimum NTs performance in terms of measured photocurrent corresponds to the anodizing time of 10 min at 45 V and thermal treatment of 3 h at 450 °C. On the other hand, maintaining the same anodization conditions, the raising of time and temperature of the thermal treatment does not improve the photoanode performance. It is also interesting to mention that the

Table 1b — Fitting parameters of EIS spectra recorded in 0.5 M Na₂SO₄ at pH 2 using Pt mesh as the counter and the working electrode recorded at various potentials with 0.1 M glycerol.

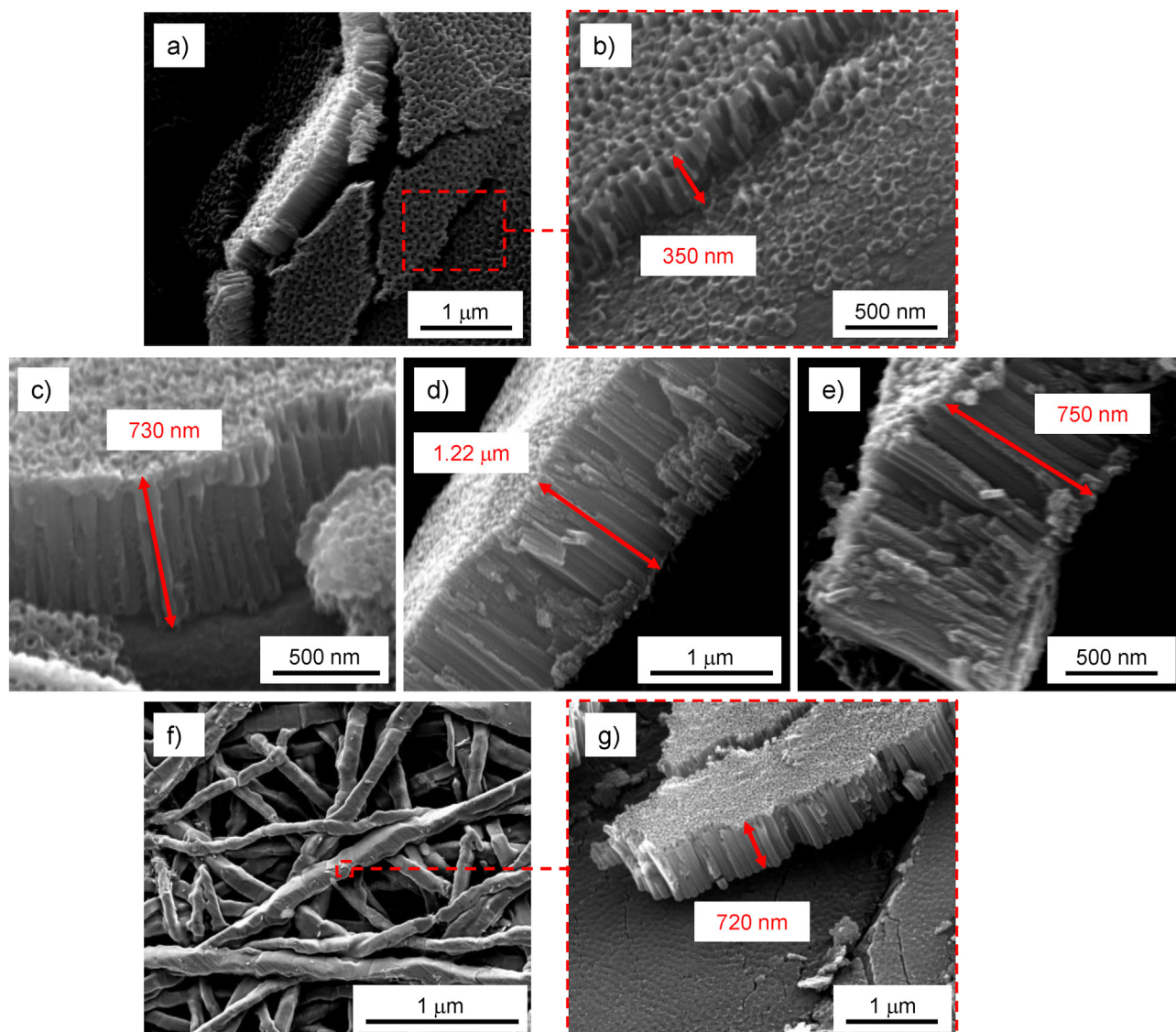| Applied potential [V vs ag/AgCl]	R_{el} [Ω cm^2]	R_{ct} [Ω cm^2]	$Q_{DL,\,el}$ [S s^n cm^{-2}]	n	χ square [adm]
0.9	4.13	9740	$1.04 \cdot 10^{-4}$	0.918	0.0259
1.1	3.97	6505	$1.03 \cdot 10^{-4}$	0.949	0.0284
1.3	3.96	1028	$1.07 \cdot 10^{-4}$	0.945	0.0316
1.5	3.93	180	$1.2 \cdot 10^{-4}$	0.9225	0.0364

Fig. 3 − SEM pictures of TiO$_2$ NTs synthesized at different conditions. a), b) anodization step (AS) 5 min at 45 V, thermal treatment (TT) of 3 h at 450 °C on Ti foil. c) AS 10 min at 45 V, TT of 3 h at 450 °C on Ti foil. d) AS 20 min at 45 V, TT of 3 h at 450 °C on Ti foil. e) AS 10 min at 45 V, TT of 12 h at 550 °C on Ti foil. f), g) AS 10 min at 45 V, TT of 3 h at 450 °C on Ti felt.

amounts of DHA and GA produced during the overall process in 5 h are not strongly dependent on the NTs features.

After this preliminary screening, larger photoanodes (the irradiated area has been increased from 24 cm^2 to 90 cm^2) were synthesized (10 min at 45 V and thermal treatment of 3 h at 450 °C) to better collect the light irradiation on both Ti foil and Ti felt. The cathode surface was also increased from 8 cm^2 to 180 cm^2 to allow a better distribution of the current lines and to reduce the cathodic current density and thus the corresponding necessary overvoltage. The measured photocurrent increased by ~4.3 times with Ti foil and by ~6.5 times with Ti felt (see Table 3). In the attempt to enhance the glycerol mass transfer inside the NTs of Ti fiber felt, the initial glycerol concentration was increased up to 0.5 M, resulting in I$_{ph}$ up to 82.8 mA (Table 3), while further increasing of the biomass concentration did not provide I$_{ph}$ enhancement. The maximum H$_2$ amount was 7.72 mmol after 5h of reaction.

Based on the experiments carried out using Ti felt as photoanode and an initial glycerol concentration of 0.1 M, after 5 h of irradiation glycerol conversion is ~13.6%, with a selectivity of 6.7% towards DHA and 19.8% towards GA. Since this is a photoelectrochemical process, we expect that the longer is the polarization the higher will be the conversion.

Table 4 summarizes the DHA, GDA, and H$_2$ production rate, normalized for incident photonic flux as well as the faradaic efficiency to allow a comparison with the previous results reported in the literature. The H$_2$ production rate normalized for both the incident photon flux and the photoanode area is one order of magnitude greater than that reported in other works.
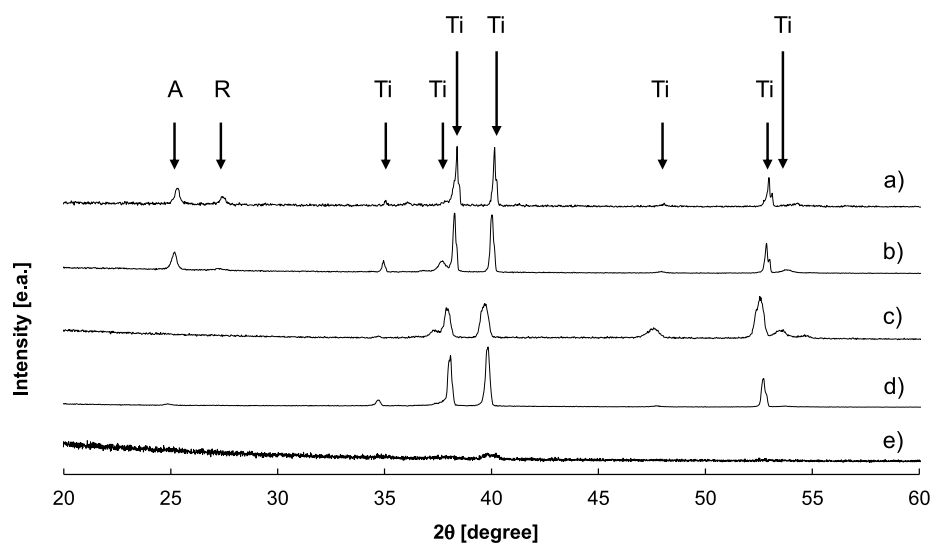
Fig. 4 – XRD patterns of TiO₂ photoanodes synthesized at different conditions: a) anodization step (AS) 10 min at 45 V, thermal treatment (TT) of 12 h at 550 °C on Ti foil, b) AS 20 min at 45V TT of 3 h at 450 °C on Ti foil, c) AS 10 min at 45V TT of 3 h at 450 °C on Ti foil, d) AS 5 min at 45V TT of 3 h at 450 °C on Ti foil and e) AS 10 min at 45V TT of 3 h at 450 °C on Ti felt.

In an attempt to explain these results, the energetic sketch of the TiO₂ NTs-electrolyte interface was built (see Fig. 7). The location of characteristic energy levels of the junction (Fermi level, E_F, conduction, and valence band edges) was carried out by considering the flat band potential derived from the photocurrent vs potential plot at 320 nm (Fig. 6c). Indeed, it is possible to locate semiconductor Fermi level, E_F, by knowing the flat band potential, V_{FB}, according to Eq. (4) [69].
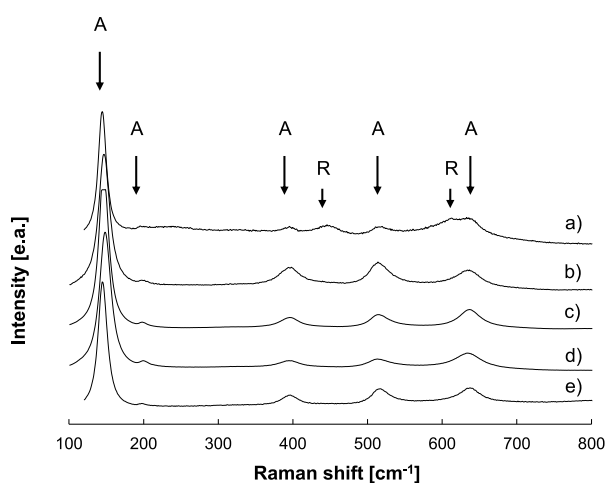

Fig. 5 – Raman spectra of TiO₂ photoanodes synthesized at different conditions: a) anodization step (AS) 10 min at 45 V, thermal treatment (TT) of 12 h at 550 °C on Ti foil, b) AS 5 min at 45V TT of 3 h at 450 °C on Ti foil, c) AS 10 min at 45V TT of 3 h at 450 °C on Ti foil, d) AS 20 min at 45V TT of 3 h at 450 °C on Ti foil and e) AS 10 min at 45V TT of 3 h at 450 °C on Ti felt.

$$E_F = -|e|V_{fb} + |e|V_{ref} \qquad (4)$$

where V_{ref} is the potential of the reference electrode used in the photoelectrochemical measurements.

After the location of the conduction band edge of oxide around 0.2 eV above E_F (in agreement with the semiconductor behavior of TiO₂ NTs), the valence band edge was determined by considering the estimated band gap mentioned above.

The high oxidizing capacity of the formed holes at the metal oxide electrolyte interface can be attributed to the distance between the valence band edge and the redox potential for glycerol and water oxidation, of 1.3 eV and 1.1 eV respectively (see Fig. 7). This can allow both water photo splitting and biomass photo reforming. Moreover, despite the low selectivity toward DHA and GA, the production rate of these high-value-added products is comparable to those reported in [33], where the formation of a Bi₂O₃/TiO₂ heterojunction allows to reduce the potential of the photogenerated holes and thus to reduce OER and glycerol mineralization to CO₂ (see Eqn. (3)).

These photoanodes are very stable both from a chemical and a mechanical point of view. Indeed, they were used for at least 10 runs (each run lasted 5 h) without suffering any damage or poisoning effect thanks to the mechanical properties of the titanium support and to the absence of Pt and/or Pt group metals which are very sensitive to the presence of CO species. Moreover, no appreciable changes were detected in their morphology, structure, and composition according to SEM, Raman, XRD analyses and measured photocurrent after the experiments (see supplementary information).

Fig. 8 shows EIS spectra recorded in 0.5 M Na₂SO₄ at pH 2 by applying 1 V between the anode and cathode, using TiO₂ NTs as the working electrode and Ni foam as the counter electrode. Fig. 8a and b shows EIS spectra recorded using TiO₂ NTs sample on Ti foil, glycerol concentration of 0.1 M with and without UV irradiation, respectively. Fig. 8 c and d show EIS
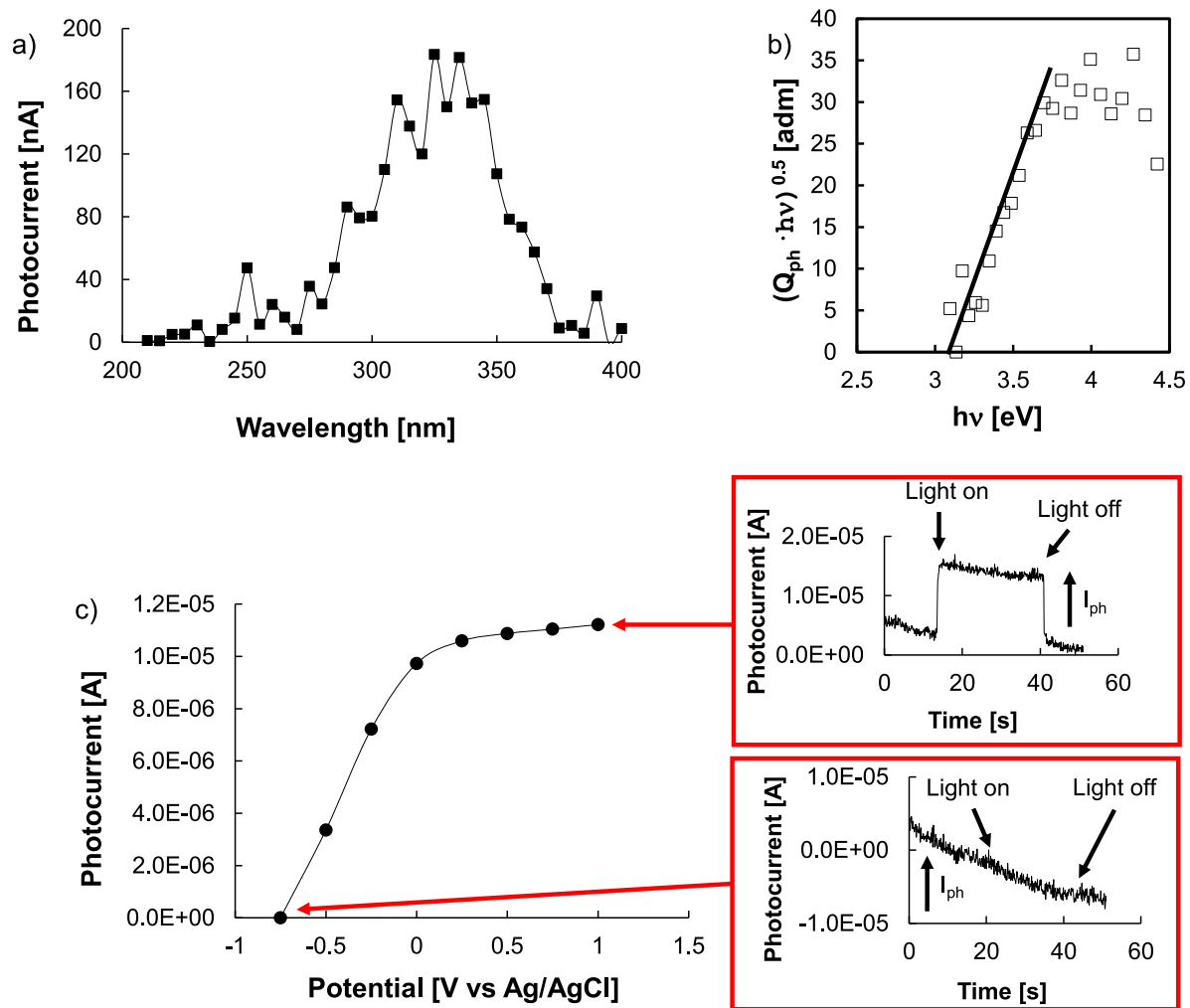
Fig. 6 – **a) Photocurrent spectra of TiO$_2$ NTs on Ti felt recorded in 0.5 M Na$_2$SO$_4$ at pH 2 and applied potential of 0.5 V vs Ag/AgCl, the respective (Q$_{ph}$·hν)$^{0.5}$ vs hν plot is shown in b). Current transient under monochromatic light recorded at 320 nm and applied potential from 1 to −0.75 V vs Ag/AgCl with a step of 0.25 V are reported in c), respective photocurrent vs time plots recorded at 1 and -0.75 V vs Ag/AgCl are reported in the inset.**

spectra recorded using TiO$_2$ NTs sample on Ti felt with and without UV irradiation, respectively, and glycerol concentrations of 0.1 M, 0.5 M, and without glycerol. All spectra were fitted using the equivalent circuit shown in Fig. 8e, where R$_s$ is the solution resistance, R$_{ct}$ is the charge transfer resistance, Q$_{SC, el}$ accounts for the capacitance of the n-type SC TiO$_2$, and C$_{Brug}$ is the TiO$_2$ capacitance calculated by the Brug formula in Eqn. (5) [72].

Table 2 – Results of the tests executed using TiO$_2$ NTs on Ti foil varying the photoanode synthesis conditions, photoanodes irradiated surface was 24 cm^2. TT = thermal treatment step, I$_{ph}$ = photocurrent, FE = Faradaic efficiency, DHA = 1,3-dihydroxyacetone, GA = glyceraldehyde. The reaction time of each test was 5 h.

Anodizing conditions	10 min at 45 V	10 min at 45 V	5 min at 45 V	20 min at 45 V	10 min at 45 V
TT	3 h at 450 °C	3 h at 450 °C	3 h at 450 °C	3 h at 450 °C	12 h at 550 °C
Glycerol concentration [M]	0	0.1	0.1	0.1	0.1
I$_{ph}$ [mA]	9.44	12.3	3.88	11.1	7.78
DHA [mmol]		$3.54 \cdot 10^{-2}$	$3.3 \cdot 10^{-2}$	$3.5 \cdot 10^{-2}$	$3.16 \cdot 10^{-2}$
FE DHA [%]		3.09	9.16	2.37	2.18
GA [mmol]		$3.62 \cdot 10^{-2}$	$3.5 \cdot 10^{-2}$	$3.9 \cdot 10^{-2}$	$3.08 \cdot 10^{-2}$
FE GA [%]		11.7	9.68	3.81	4.26
CO$_2$ [mmol]		$5.65 \cdot 10^{-3}$	$2.3 \cdot 10^{-5}$	$3.3 \cdot 10^{-3}$	$3.7 \cdot 10^{-3}$
FE CO$_2$ [%]		3.47	0.045	2.09	3.59
H$_2$ [mmol]	0.88	1.15	0.362	1.03	0.726

Table 3 − Results of the tests executed using TiO₂ NTs on Ti foil and Ti felt, obtained through an anodization step of 10 min at 45 V and a thermal treatment step of 3 h at 450 °C. Photoanodes irradiated surface was 90 cm², I_{ph} = photocurrent, FE = Faradaic efficiency, DHA = 1,3-dihydroxyacetone, GA = glyceraldehyde. The reaction time of each test was 5 h.

Substrate	Ti foil	Ti foil	Ti felt	Ti felt	Ti felt
Initial glycerol [M]	0	0.1	0	0.1	0.5
I_{ph} [mA]	41.7	53.3	50.0	80.5	82.8
DHA [mmol]		0.184		0.218	0.36
FE DHA [%]		3.12		2.74	3.39
GA [mmol]		0.518		0.605	0.493
FE GA [%]		10.4		8.07	6.39
CO_2 [mmol]		$7.62 \cdot 10^{-2}$		0.141	0.15
FE CO_2 [%]		10.7		13.2	13.6
H_2 [mmol]	3.89	4.97	4.66	7.51	7.72

Table 4 − H_2, DHA, and GA production rate related to incident photon flux and photoanode found in this work and comparison with data found in the literature.

| Ref.	[70]	[71]	[33]	This work
Photoanode	$BiVO_4$	$NiO_x(OH)_y/W:BiVO_4$	Bi_2O_3/TiO_2	TiO_2
Cathode	Pt		Pt	Ni foam
Electrolyte	Glycerol 2 M 0.1 M $Na_2B_4O_7$ pH 9.4	Glycerol 0.1 M 0.5 M KBi pH = 9.3	Glycerol 0.1 M 0.5 M Na_2SO_4 pH = 2	Glycerol 0.1 M 0.5 M Na_2SO_4 pH = 2
Applied bias	0.7 V vs RHE	1.2 V vs. RHE	2 V	1 V
Photoanode area [cm²]	4	−	7	90
Light source [mW cm⁻²]	100	100	100	10
DHA production rate [μmol h⁻¹ mW⁻¹]	$4.2 \cdot 10^{-2}$	$13.8 \cdot 10^{-2}$	$17.2 \cdot 10^{-2}$	$4.84 \cdot 10^{-2}$
GA production rate [μmol h⁻¹ mW⁻¹]	n.a.	0 (0.1 in 0.5 M Na_2SO_4 electrolyte)	0.28	0.134
H_2 production rate [μmol h⁻¹ mW⁻¹]	0.0833	0.40	0.155	1.67
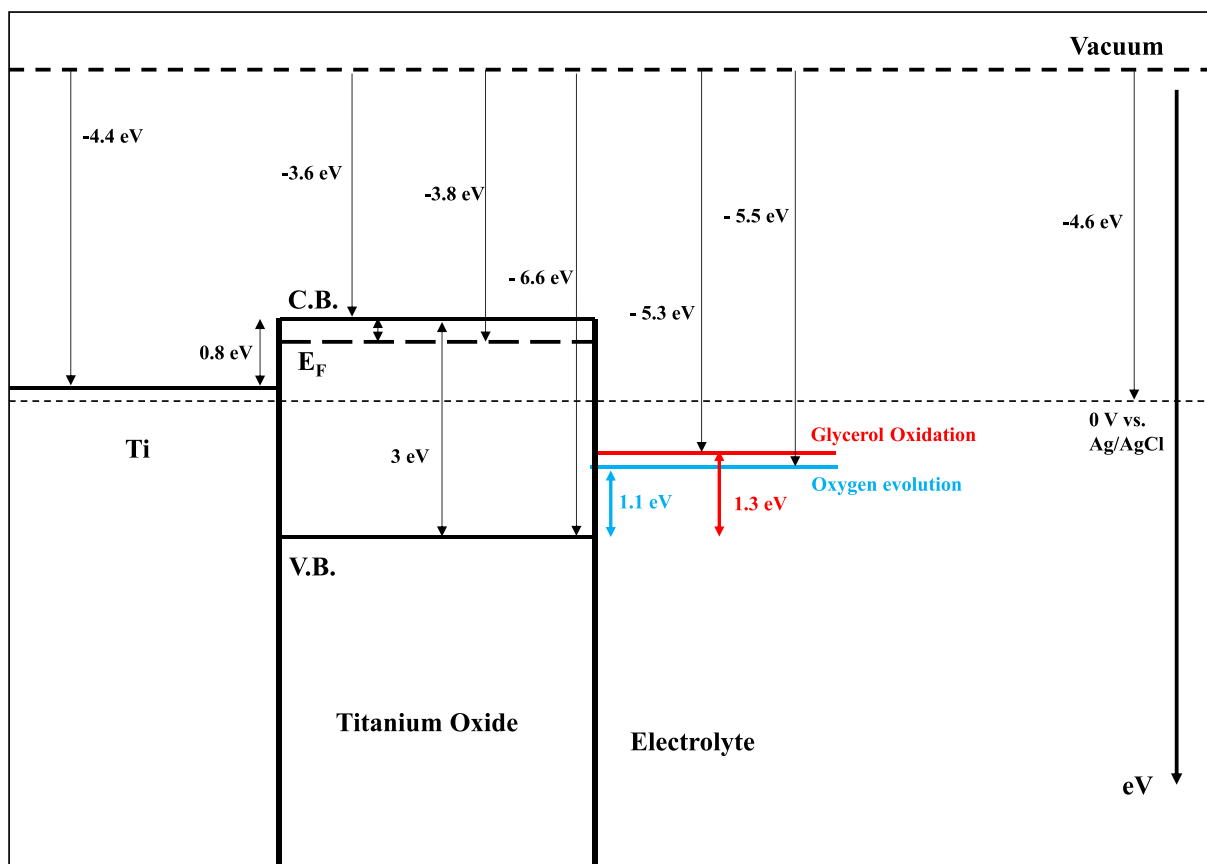
Fig. 7 − Sketch of the energetic levels of the metal/oxide/electrolyte interface.
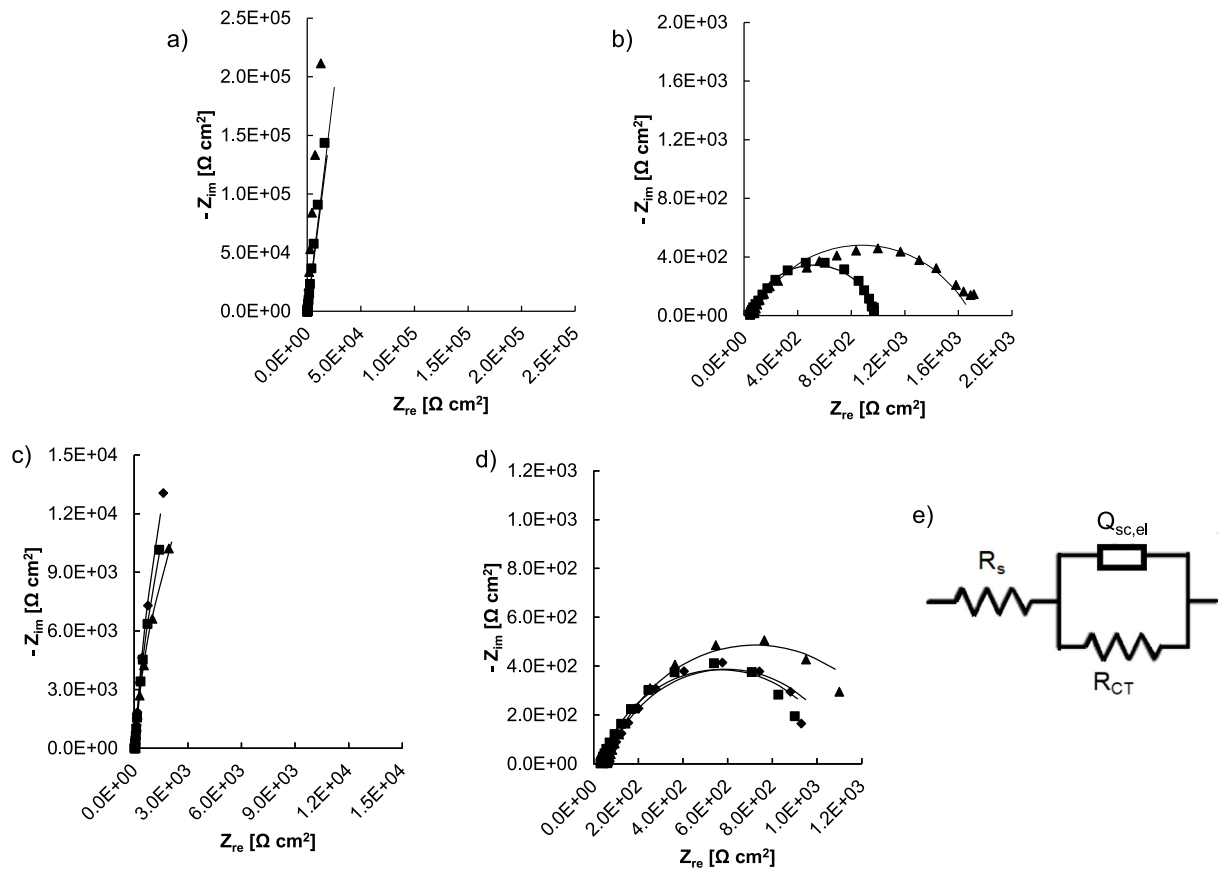
Fig. 8 — **EIS spectra performed in 0.5 M Na₂SO₄ electrolyte at pH 2 using TiO₂ NTs on Ti foil or Ti felt and Ni foam as the counter electrode. a) and b) show EIS spectra recorded using TiO₂ nts on Ti foil without and with UV irradiation, respectively, and glycerol concentration of (■) 0.1 M, and (▲) without glycerol. c) and d) show EIS spectra recorded using TiO₂ NTs on Ti felt without and with UV irradiation, respectively, and glycerol concentration of (■) 0.1 M, (♦) 0.5 M, and (▲) without glycerol. All spectra were fitted using the model shown in e).**

Table 5 — Fitting parameters of EIS spectra recorded using TiO₂ photoanodes and Ni foam as the cathode. TiO₂ NTs were obtained through an anodization step of 10 min at 45 V and a thermal treatment step of 3 h at 450 °C. EIS spectra were recorded in 0.5 M Na₂SO₄ at pH 2 by applying 1 V between the anode and cathode, results were obtained with and without UVA irradiation.

Photoanode	R_s [Ω cm^2]	R_{ct} [Ω cm^2]	$Q_{SC, el}$ [μS s^n cm^{-2}]	n	C_{Brug} [μF cm^{-2}]	χ square [adm]
TiO₂ NTs on Ti foil Glycerol 0 M Dark	83	$5.1\cdot10^5$	8.0	0.916	4.09	$1.88\cdot10^{-2}$
TiO₂ NTs on Ti foil Glycerol 0 M Light	58	1644	46.0	0.674	2.62	$6.92\cdot10^{-3}$
TiO₂ NTs on Ti foil Glycerol 0.1 M Dark	49	$6.49\cdot10^6$	11.4	0.911	5.48	$1.04\cdot10^{-2}$
TiO₂ NTs on Ti foil Glycerol 0.1 M Light	43	970	90.3	0.779	18.7	$2.64\cdot10^{-3}$
TiO₂ NTs on Ti felt Glycerol 0 M Dark	71	$7.86\cdot10^4$	140	0.966	119	$1.41\cdot10^{-3}$
TiO₂ NTs on Ti felt Glycerol 0 M Light	61	1326	500	0.8068	216	$1.78\cdot10^{-3}$
TiO₂ NTs on Ti felt Glycerol 0.1 M Dark	33	$1.48\cdot10^5$	150	0.957	118	$1.13\cdot10^{-2}$
TiO₂ NTs on Ti felt Glycerol 0.1 M Light	31	1070	480	0.796	163	$2.02\cdot10^{-2}$
TiO₂ NTs on Ti felt Glycerol 0.5 M Dark	61.2	$1.86\cdot10^5$	130	0.967	110	$3.3\cdot10^{-2}$
TiO₂ NTs on Ti felt Glycerol 0.5 M Light	58.4	1074	460	0.796	182	$2.85\cdot10^{-2}$

$$C_{Brug} = Q_{SC,el}^{(1/n)} \left(\frac{R_s\ R_{ct}}{R_s + R_{ct}} \right)^{\frac{(1-n)}{n}} \tag{5}$$

The parameters obtained by a best-fitting procedure are reported in Table 5.

It is evident that light irradiation significantly affects the behavior of the electrode/electrolyte interface. Indeed, the charge transfer resistance (R_{ct}) measured in the dark for all the investigated photoanodes is very high and the best fitting exponent n for the $Q_{sc,\ el}$ is close to 1, as expected for an almost ideal n-type semiconductor, which results to be blocking toward the electronic current. Notably, the capacitance calculated by the Brug formula shown in Table 5 depends on the kind of photoanode and since the TiO_2 layers were grown by the same anodizing process and were subjected to the same thermal treatment, the different capacitance can be attributed to a different specific surface. Therefore, the real active surface of TiO_2 NTs grown on Ti felt is higher than that of the TiO_2 NTs grown on the foil. This is still true even after light irradiation in agreement with the higher photocurrent measured by using the felt.

Soon after irradiation, a significant reduction of R_{ct} occurs strictly linked to the enhanced photocarrier concentration and in agreement with the higher capacitance. However, under illumination, lower R_{ct} and higher photocurrent were measured in 0.1 M glycerol-containing solution than that estimated in glycerol-free solution, indicating that the overall reaction is less demanding from a kinetic point of view.

4. Conclusions

Photoelectrochemical H_2 production in PGM-free cells by water and glycerol photo-oxidation was studied using TiO_2 NTs on Ti foil as photoanode and Ni foam as cathode with working areas ranging from 24 to 90 cm^2 and from 6 to 180 cm^2, respectively.

Photoelectrocatalytic tests carried out in acidic aqueous solutions revealed that the presence of glycerol allowed to get an enhancement of the measured photocurrent resulting in a higher H_2 production rate and in the formation of high-value added oxidation products (i.e. DHA and GA). The best results were obtained with TiO_2 NTs ~730 nm long annealed for 3 h at 450 °C. Consequently, photoanodes with a higher surface were prepared under the same conditions for better collecting light irradiation.

Further improvements were obtained by using high specific surface Ti fiber felt as substrate and increasing initial glycerol concentration up to 0.5 M. A H_2 production rate of 1.67 $\mu mol\ h^{-1}\ mW^{-1}$ was obtained resulting significantly higher with respect to previous results reported in the literature. Moreover, DHA and GA were also produced by the photo-oxidation of glycerol even if with a faradaic efficiency lower with respect to the value reported for functionalized TiO_2 electrodes.

The obtained results are encouraging if it is also considered that both photoanode and cathode can be used for a not limited number of runs, due to their high mechanical and chemical stability and reproducibility in the reaction conditions.

Declaration of competing interest

The authors declare that they have no known competing financial interests or personal relationships that could have appeared to influence the work reported in this paper.

Acknowledgments

Appendix A. Supplementary data

Supplementary data to this article can be found online at https://doi.org/10.1016/j.ijhydene.2023.08.011.

REFERENCES

[1] IRENA. Making the breakthrough: green hydrogen policies and technology costs. 2021.

[2] Maslova V, Fasolini A, Offidani M, Albonetti S, Basile F. Solar-driven valorization of glycerol towards production of chemicals and hydrogen. Catal Today 2021;380:147–55. https://doi.org/10.1016/j.cattod.2021.03.008.

[3] Michal R, Sfaelou S, Lianos P. Photocatalysis for renewable energy production using PhotoFuelCells. Molecules 2014;19:19732–50. https://doi.org/10.3390/MOLECULES191219732. 2014;19:19732–50.

[4] Holladay JD, Hu J, King DL, Wang Y. An overview of hydrogen production technologies. Catal Today 2009;139:244–60. https://doi.org/10.1016/j.cattod.2008.08.039.

[5] Li Y, Bahamon D, Sinnokrot M, Al-Ali K, Palmisano G, Vega LF. Computational modeling of green hydrogen generation from photocatalytic H2S splitting: overview and perspectives. J Photochem Photobiol C Photochem Rev 2021;49:100456. https://doi.org/10.1016/j.jphotochemrev.2021.100456.

[6] González-Garay A, mac Dowell N, Shah N. A carbon neutral chemical industry powered by the sun. Discover Chemical Engineering 2021;1:2. https://doi.org/10.1007/s43938-021-00002-x.

[7] Panchenko VA, Daus YV, Kovalev AA, Yudaev IV, Litti YV. Prospects for the production of green hydrogen: review of countries with high potential. Int J Hydrogen Energy 2023;48:4551–71. https://doi.org/10.1016/J.IJHYDENE.2022.10.084.

[8] Eicke L, De Blasio N. Green hydrogen value chains in the industrial sector—geopolitical and market implications. Energy Res Social Sci 2022;93:102847. https://doi.org/10.1016/J.ERSS.2022.102847.

[9] Kakoulaki G, Kougias I, Taylor N, Dolci F, Moya J, Jäger-Waldau A. Green hydrogen in Europe – a regional assessment: substituting existing production with electrolysis powered by renewables. Energy Convers Manag 2021;228:113649. https://doi.org/10.1016/J.ENCONMAN.2020.113649.

[10] IRENA. Green hydrogen cost reduction: scaling up electrolysers to meet the 1.5°C climate goal. 2020.

[11] Semente ABS, Madeira Rodrigues CB, Mariano MA, Gaspar MB, Šljukić B, Santos DMF. Prospects and challenges for the green hydrogen market. Solar-Driven Green

Hydrogen Generation and Storage 2023:381–415. https://doi.org/10.1016/B978-0-323-99580-1.00021-2.

[12] Ishaq H, Dincer I, Crawford C. A review on hydrogen production and utilization: challenges and opportunities. Int J Hydrogen Energy 2022;47:26238–64. https://doi.org/10.1016/J.IJHYDENE.2021.11.149.

[13] Velazquez Abad A, Dodds PE. Green hydrogen characterisation initiatives: definitions, standards, guarantees of origin, and challenges. Energy Pol 2020;138:111300. https://doi.org/10.1016/J.ENPOL.2020.111300.

[14] Ghanashyam G, Kyung Jeong H. Flower-like molybdenum disulfide for efficient hydrogen and oxygen evolution reaction. Inorg Chim Acta 2022;541:121098. https://doi.org/10.1016/J.ICA.2022.121098.

[15] She L, Zhao G, Ma T, Chen J, Sun W, Pan H. On the durability of iridium-based electrocatalysts toward the oxygen evolution reaction under acid environment. Adv Funct Mater 2022;32:2108465. https://doi.org/10.1002/ADFM.202108465.

[16] Yu M, Budiyanto E, Tüysüz H. Principles of water electrolysis and recent progress in cobalt-, nickel-, and iron-based oxides for the oxygen evolution reaction. Angew Chem Int Ed 2022;61:e202103824. https://doi.org/10.1002/ANIE.202103824.

[17] Lin X, Wang J. Green synthesis of well dispersed TiO2/Pt nanoparticles photocatalysts and enhanced photocatalytic activity towards hydrogen production. Int J Hydrogen Energy 2019;44:31853–9. https://doi.org/10.1016/J.IJHYDENE.2019.10.062.

[18] Davis KA, Yoo S, Shuler EW, Sherman BD, Lee S, Leem G. Photocatalytic hydrogen evolution from biomass conversion. Nano Convergence 2021;8:1. https://doi.org/10.1186/S40580-021-00256-9. 2021;8:1–19.

[19] Augustin A, Chuaicham C, Shanmugam M, Vellaichamy B, Rajendran S, Hoang TKA, et al. Recent development of organic–inorganic hybrid photocatalysts for biomass conversion into hydrogen production. Nanoscale Adv 2022;4:2561–82. https://doi.org/10.1039/D2NA00119E.

[20] Bellardita M, Palmisano L, Loddo V. Boosting high added-value chemicals formation by means of photoelectrocatalysis. Journal of Photocatalysis 2022;3. https://doi.org/10.2174/2665976x03666220513153344.

[21] Gallezot P. Conversion of biomass to selected chemical products. Chem Soc Rev 2012;41:1538–58. https://doi.org/10.1039/C1CS15147A.

[22] Werpy TA, Holladay JE, White JF. Top value added chemicals from biomass: I. Results of screening for potential candidates from sugars and synthesis gas. 2004. https://doi.org/10.2172/926125. Richland, WA.

[23] Espro C, Paone E, Mauriello F, Gotti R, Uliassi E, Bolognesi ML, et al. Sustainable production of pharmaceutical, nutraceutical and bioactive compounds from biomass and waste. Chem Soc Rev 2021;50:11191–207. https://doi.org/10.1039/D1CS00524C.

[24] Pecoraro CM, Bellardita M, Loddo V, Virtù D, Di Franco F, Santamaria M. Photocatalytic and photoelectrocatalytic H2 evolution combined with valuable furfural production. Appl Catal Gen 2023;650:118987. https://doi.org/10.1016/j.apcata.2022.118987.

[25] Sanwald KE, Berto TF, Jentys A, Camaioni DM, Gutiérrez OY, Lercher JA. Kinetic coupling of water splitting and photoreforming on SrTiO3-based photocatalysts. ACS Catal 2018;8:2902–13. https://doi.org/10.1021/ACSCATAL.7B03192/SUPPL_FILE/CS7B03192_SI_001.PDF.

[26] Serrano-Ruiz JC, Luque R, Sepúlveda-Escribano A. Transformations of biomass-derived platform molecules: from high added-value chemicals to fuelsvia aqueous-phase processing. Chem Soc Rev 2011;40:5266–81. https://doi.org/10.1039/C1CS15131B.

[27] Christensen CH, Rass-Hansen J, Marsden CC, Taarning E, Egeblad K. The renewable chemicals industry. ChemSusChem 2008;1:283–9. https://doi.org/10.1002/CSSC.200700168.

[28] Shi Q, Duan H. Recent progress in photoelectrocatalysis beyond water oxidation. Chem Catal 2022;2:3471–96. https://doi.org/10.1016/j.checat.2022.11.007.

[29] Yu J, González-Cobos J, Dappozze F, López-Tenllado FJ, Hidalgo-Carrillo J, Marinas A, et al. WO3-based materials for photoelectrocatalytic glycerol upgrading into glyceraldehyde: unravelling the synergistic photo- and electro-catalytic effects. Appl Catal, B 2022;318:121843. https://doi.org/10.1016/J.APCATB.2022.121843.

[30] Fan L, Liu B, Liu X, Senthilkumar N, Wang G, Wen Z. Recent progress in electrocatalytic glycerol oxidation. Energy Technol 2021;9:2000804. https://doi.org/10.1002/ENTE.202000804.

[31] Pecoraro CM, Bellardita M, Loddo V, Di Franco F, Palmisano L, Santamaria M. A facile way to synthesize noble metal free TiO2 based catalysts for glycerol photoreforming. J Ind Eng Chem 2023;118:247–58. https://doi.org/10.1016/j.jiec.2022.11.010.

[32] Ciriminna R, Fidalgo A, Ilharco LM, Pagliaro M. Dihydroxyacetone: an updated insight into an important bioproduct. Chemistry 2018;7:233–6. https://doi.org/10.1002/open.201700201.

[33] Luo L, Chen W, Xu S-M, Yang J, Li M, Zhou H, et al. Selective photoelectrocatalytic glycerol oxidation to dihydroxyacetone via enhanced middle hydroxyl adsorption over a Bi$_2$O$_3$-incorporated catalyst. J Am Chem Soc 2022;144:7720–30. https://doi.org/10.1021/jacs.2c00465.

[34] Verma AM, Laverdure L, Melander MM, Honkala K. Mechanistic origins of the pH dependency in Au-catalyzed glycerol electro-oxidation: insight from first-principles calculations. ACS Catal 2022;12:662–75. https://doi.org/10.1021/ACSCATAL.1C03788/ASSET/IMAGES/LARGE/CS1C03788_0006.JPEG.

[35] Liu Y, Wang M, Zhang B, Yan D, Xiang X. Mediating the oxidizing capability of surface-bound hydroxyl radicals produced by photoelectrochemical water oxidation to convert glycerol into dihydroxyacetone. ACS Catal 2022;12:6946–57. https://doi.org/10.1021/ACSCATAL.2C01319/ASSET/IMAGES/LARGE/CS2C01319_0007.JPEG.

[36] Çetinkaya S, Khamidov G, Özcan L, Palmisano L, Yurdakal S. Selective photoelectrocatalytic oxidation of glycerol by nanotube, nanobelt and nanosponge structured TiO2 on Ti plates. J Environ Chem Eng 2022;10:107210. https://doi.org/10.1016/j.jece.2022.107210.

[37] Bessegato GG, Guaraldo TT, de Brito JF, Brugnera MF, Zanoni MVB. Achievements and trends in photoelectrocatalysis: from environmental to energy applications. Electrocatalysis 2015;6:415–41. https://doi.org/10.1007/S12678-015-0259-9. 2015 6:5.

[38] Yao T, An X, Han H, Chen JQ, Li C. Photoelectrocatalytic materials for solar water splitting. Adv Energy Mater 2018;8:1800210. https://doi.org/10.1002/AENM.201800210.

[39] Grätzel M. Photoelectrochemical cells. Nature 2001;414:338–44.

[40] Pitchaimuthu S, Sridharan K, Nagarajan S, Ananthraj S, Robertson P, Kuehnel MF, et al. Solar hydrogen fuel generation from wastewater—beyond photoelectrochemical water splitting: a perspective. Energies 2022;15. https://doi.org/10.3390/EN15197399.

[41] Li T, Mo JY, Weekes DM, Dettelbach KE, Jansonius RP, Sammis GM, et al. Photoelectrochemical decomposition of lignin model compound on a BiVO4 photoanode.

ChemSusChem 2020;13:3622–6. https://doi.org/10.1002/CSSC.202001134.

[42] Sun Y, Han G, Du L, Du C, Zhou X, Sun Q, et al. Photoelectrochemistry-driven selective hydroxyl oxidation of polyols: synergy between Au nanoparticles and C3N4 nanosheets. Chem Catal 2021;1:1260–72. https://doi.org/10.1016/J.CHECAT.2021.09.001.

[43] Yu J, González-Cobos J, Dappozze F, López-Tenllado FJ, Hidalgo-Carrillo J, Marinas A, et al. WO3-based materials for photoelectrocatalytic glycerol upgrading into glyceraldehyde: unravelling the synergistic photo- and electro-catalytic effects. Appl Catal, B 2022;318. https://doi.org/10.1016/J.APCATB.2022.121843.

[44] Jakubow-Piotrowska K, Witkowski B, Augustynski J. Photoelectrocatalytic hydrogen generation coupled with reforming of glucose into valuable chemicals using a nanostructured WO3 photoanode. Commun Chem 2022;5. https://doi.org/10.1038/s42004-022-00745-w.

[45] Lianos P. Review of recent trends in photoelectrocatalytic conversion of solar energy to electricity and hydrogen. Appl Catal, B 2017;210:235–54. https://doi.org/10.1016/j.apcatb.2017.03.067.

[46] Miao Y, Li Z, Song Y, Fan K, Guo J, Li R, et al. Surface active oxygen engineering of photoanodes to boost photoelectrochemical water and alcohol oxidation coupled with hydrogen production. Appl Catal, B 2023:323. https://doi.org/10.1016/j.apcatb.2022.122147.

[47] Govind Rajan A, Martirez JMP, Carter EA. Why do we use the materials and operating conditions we use for heterogeneous (Photo)Electrochemical water splitting? ACS Catal 2020;10. https://doi.org/10.1021/ACSCATAL.0C01862.

[48] Dey A, Houle FA, Lubner CE, Sevilla M, Shaw WJ. Introduction to (photo)electrocatalysis for renewable energy. Chem Commun 2021;57:1540–2. https://doi.org/10.1039/D0CC90530E.

[49] Yu J, González-Cobos J, Dappozze F, Grimaldos-Osorio N, Vernoux P, Caravaca A, et al. First PEM photoelectrolyser for the simultaneous selective glycerol valorization into value-added chemicals and hydrogen generation. Appl Catal, B 2023;327. https://doi.org/10.1016/j.apcatb.2023.122465.

[50] Han Y, Chang M, Zhao Z, Niu F, Zhang Z, Sun Z, et al. Selective valorization of glycerol to formic acid on a BiVO4 photoanode through NiFe phenolic networks. ACS Appl Mater Interfaces 2023;15:11678–90. https://doi.org/10.1021/acsami.2c20516.

[51] Nascimento LL, Marinho JZ, dos Santos ALR, de Faria AM, Souza RAC, Wang C, et al. Photoelectrochemical reforming of glycerol by Bi2WO6 photoanodes: role of the electrolyte pH on the H2 evolution efficiency and product selectivity. Appl Catal Gen 2022;646. https://doi.org/10.1016/j.apcata.2022.118867.

[52] Lin C, Dong C, Kim S, Lu Y, Wang Y, Yu Z, et al. Photo-electrochemical glycerol conversion over a mie scattering effect enhanced porous BiVO4 photoanode. Adv Mater 2023. https://doi.org/10.1002/adma.202209955.

[53] Eidsvåg H, Bentouba S, Vajeeston P, Yohi S, Velauthapillai D. TiO2 as a photocatalyst for water splitting—an experimental and theoretical review. Molecules 2021;26:1687. https://doi.org/10.3390/molecules26061687.

[54] Wang Y, Zu M, Zhou X, Lin H, Peng F, Zhang S. Designing efficient TiO2-based photoelectrocatalysis systems for chemical engineering and sensing. Chem Eng J 2020;381:122605. https://doi.org/10.1016/J.CEJ.2019.122605.

[55] Zhao Y, Chang W, Huang Z, Feng X, Ma L, Qi X, et al. Enhanced removal of toxic Cr(VI) in tannery wastewater by photoelectrocatalysis with synthetic TiO2 hollow spheres. Appl Surf Sci 2017;405:102–10. https://doi.org/10.1016/J.APSUSC.2017.01.306.

[56] Djaballah AM, Bellardita M, Palmisano L, Loddo V, Umair M, Pecoraro CM, et al. Facile preparation of CuBi2O4/TiO2 hetero-systems employed for simulated solar-light selective oxidation of 4-methoxybenzyl alcohol model compound. Mol Catal 2023;546:113251. https://doi.org/10.1016/j.mcat.2023.113251.

[57] Grozovski V, Climent V, Herrero E, Feliu JM. Intrinsic activity and poisoning rate for HCOOH oxidation at Pt(100) and vicinal surfaces containing monoatomic (111) steps. ChemPhysChem 2009;10:1922. https://doi.org/10.1002/cphc.200900261. –6.

[58] Santamaria M, Conigliaro G, di Franco F, di Quarto F. Photoelectrochemical evidence of Cu2O/TiO2Nanotubes hetero-junctions formation and their physicochemical characterization. Electrochim Acta 2014;144:315–23. https://doi.org/10.1016/j.electacta.2014.07.154.

[59] Kowalski D, Kim D, Schmuki P. TiO2 nanotubes, nanochannels and mesosponge: self-organized formation and applications. Nano Today 2013;8:235–64. https://doi.org/10.1016/j.nantod.2013.04.010.

[60] Roy P, Berger S, Schmuki P. TiO2 nanotubes: synthesis and applications. Angew Chem Int Ed 2011;50:2904–39. https://doi.org/10.1002/anie.201001374.

[61] Reyes-Coronado D, Rodríguez-Gattorno G, Espinosa-Pesqueira ME, Cab C, de Coss R, Oskam G. Phase-pure TiO$_2$ nanoparticles: anatase, brookite and rutile. Nanotechnology 2008;19:145605. https://doi.org/10.1088/0957-4484/19/14/145605.

[62] Motola M, Hromadko L, Prikryl J, Sopha H, Krbal M, Macak JM. Intrinsic properties of high-aspect ratio single- and double-wall anodic TiO2 nanotube layers annealed at different temperatures. Electrochim Acta 2020;352:136479. https://doi.org/10.1016/j.electacta.2020.136479.

[63] Santamaria M, Conigliaro G, Franco F Di, Megna B, Quarto F Di. Electronic properties of thermal oxides on Ti and their influence on impedance and photoelectrochemical behavior of TiO$_2$ nanotubes. J Electrochem Soc 2017;164:C113–20. https://doi.org/10.1149/2.0601704jes.

[64] Albu SP, Tsuchiya H, Fujimoto S, Schmuki P. TiO$_2$ nanotubes – annealing effects on detailed morphology and structure. Eur J Inorg Chem 2010;2010:4351–6. https://doi.org/10.1002/ejic.201000608.

[65] Balachandran U, Eror NG. Raman spectra of titanium dioxide. J Solid State Chem 1982;42:276–82. https://doi.org/10.1016/0022-4596(82)90006-8.

[66] Parker JC, Siegel RW. Calibration of the Raman spectrum to the oxygen stoichiometry of nanophase TiO2. Appl Phys Lett 1990;57:943–5. https://doi.org/10.1063/1.104274.

[67] Franco F di, Zaffora A, Pupillo D, Iannucci L, Grassini S, Santamaria M. The effect of electronic properties of anodized and hard anodized Ti and Ti6Al4V on their reactivity in simulated body fluid. J Electrochem Soc 2022;169:71506. https://doi.org/10.1149/1945-7111/AC8316.

[68] Zaffora A, di Franco F, di Quarto F, Santamaria M. Optimization of anodizing process of tantalum for Ta2O5-based capacitors. J Solid State Electrochem 2020;24:2953–62. https://doi.org/10.1007/S10008-020-04704-0/FIGURES/10.

[69] Di Franco F, Zaffora A, Santamaria M. Photoelectrochemical characterization of photocatalysts. Materials Science in Photocatalysis 2021:115–23. https://doi.org/10.1016/B978-0-12-821859-4.00005-2. Elsevier.

[70] Huang LW, Vo TG, Chiang CY. Converting glycerol aqueous solution to hydrogen energy and dihydroxyacetone by the BiVO4 photoelectrochemical cell. Electrochim Acta 2019;322:134725. https://doi.org/10.1016/J.ELECTACTA.2019.134725.

[71] Wu YH, Kuznetsov DA, Pflug NC, Fedorov A, Müller CR. Solar-driven valorisation of glycerol on BiVO4 photoanodes: effect of co-catalyst and reaction media on reaction selectivity. J Mater Chem A Mater 2021;9:6252–60. https://doi.org/10.1039/D0TA10480A.

[72] Hirschorn B, Orazem ME, Tribollet B, Vivier V, Frateur I, Musiani M. Determination of effective capacitance and film thickness from constant-phase-element parameters. Electrochim Acta 2010;55:6218–27. https://doi.org/10.1016/j.electacta.2009.10.065.